

# Parameter Space Exploration of Cellular Mechanical Metamaterials Using Genetic Algorithms

Sheng Liu\* o and Pınar Acar o Virginia Polytechnic Institute and State University, Blacksburg, Virginia 24061

https://doi.org/10.2514/1.J062864

Cellular materials widely exist in natural biologic systems such as honeycombs, bones, and woods. With advances in additive manufacturing, research on cellular metamaterials is emerging due to their unique mechanical performance. However, the design of on-demand cellular metamaterials usually requires solving a challenging inverse design problem for exploring complex structure–property relations of microstructured representative volume elements (RVEs) in the design domain. Here, we propose an experience-free and systematic methodology for exploring a parametrized system for microstructures of cellular mechanical metamaterials using a multiobjective genetic algorithm (GA). Globally, by considering the importance of the initial population selection for a population-based heuristic optimization method, we study the impact of the populations initialized by the different sampling methods on the optimal solutions. Locally, we develop our method by using a micro-GA with a new searching strategy, which requires the standard genetic algorithm to be conditionally run for a sufficient number of times with a small population size during the global searching process. We have applied our method to explore optimal solutions for applications mapped on two different parameter spaces of the cellular mechanical metamaterials with periodic and nonperiodic RVEs effectively and accurately.

# Nomenclature

A = direction index of node set 1

 $A_{\text{nodal}}$  = area of representative volume element front surface

B = direction index of node set 2 C = direction index of reference point

E = Young's modulus

 $F_{\text{nodal}}$  = nodal force in index direction

= objective function

 $f_{\text{best}}$  = best objective function value

H = height of the representative volume element

 $K_{\text{best}}$  = fittest individual L = side length of unit cell

 $L_{\text{tolr}}$  = distance tolerance in geometric constraint

N = population size r = polar radius U = nodal displacement

W = width of representative volume element  $\Delta \zeta_i$  = difference of *i*th porous parameter

 $\zeta$  = porous parameter

 $\zeta_{i,j}$  = *i*th porous parameter of *j*th cycle of genetic algorithm  $\zeta_{j,\text{max}}$  = maximum side length of reduced parameter space  $\zeta_{j,\text{min}}$  = minimum side length of reduced parameter space  $\zeta_{0,\text{max}}$  = maximum side length of initial parameter space  $\zeta_{0,\text{min}}$  = minimum side length of initial parameter space

 $\zeta^L$  = lower bound of porous parameter  $\zeta^U$  = upper bound of porous parameter

 $\theta$  = polar angle  $\nu$  = Poisson's ratio  $\phi$  = porosity

#### I. Introduction

C ELLULAR materials nowadays have become one of the most promising materials owing to their high strength and light

Received 1 February 2023; revision received 16 March 2023; accepted for publication 17 March 2023; published online 30 May 2023. Copyright © 2023 by Sheng Liu and Pinar Acar. Published by the American Institute of Aeronautics and Astronautics, Inc., with permission. All requests for copying and permission to reprint should be submitted to CCC at www.copyright.com; employ the eISSN 1533-385X to initiate your request. See also AIAA Rights and Permissions www.aiaa.org/randp.

weight [1]. Due to their unique features, these materials have widespread applications in aerospace [2,3] and transportation [4,5] industries as structural panels. In recent years, the advent of additive manufacturing has allowed the realization of high-performance and high-precision industrial parts and products built with cellular mechanical metamaterials (CMMs). The CMMs are assembled with representative volume elements (RVEs) in repeating patterns. Mechanical effective properties of the cellular metamaterials mainly depend on the geometric patterns of RVEs rather than the materials own chemical composites [6,7]. Consequently, the design of cellular materials is simplified as optimizing the geometric patterns of RVEs, which are periodically distributed within the design domain. To meet varied industrial requirements and realize the corresponding metamaterials, there is a need for efficient multiobjective design approaches to exploit the implicit relationship between the geometric patterns of RVEs and their corresponding properties.

In our study, the microstructure of the CMMs is parametrized, enabling a designer to tune geometric variables for specific applications in industries, corresponding to particular material properties such as Young's modulus, Poisson's ratio, porosity, etc. Traditionally, the investigation of the optimal microstructures requires repeated attempts for combinations of the geometric parameters. Without any prior information, the search is time consuming due to complex simulations or experimental approaches to evaluate the structural responses of every test microstructure [8,9]. Therefore, with the increased complexity requirements in material design, a design must have an effective method for finding a feasible set of parameter values that defines the microstructures of new materials. Recently, advances in deep learning have been beneficial for the design of new materials using various neural networks (NNs) [10,11]. However, there are several potential issues arising from using NNs for materials design: 1) the high computational expenses of building an extensive database for structure-property relations [12], 2) the number of trails and tests in constructing the architectures of NNs to avoid overfitting issues while maintaining high accuracy, and 3) difficulties in interpreting the physical meaning of the connection between the hidden neurons of NNs [13].

Considering the preceding issues, we outline an experience-free and systemic methodology using a multiobjective genetic algorithm (GA) rather than deep learning. Unlike deep learning, this GA-based computational methodology is independent of prior knowledge about the structure–property relations and searches for the optima among the realistic microstructures of RVEs. Moreover, our method employs a micro-GA with a relatively small population size as compared with a traditional GA. To avoid premature convergence in the local optimum, the optimization process will restart the GA

<sup>\*</sup>Graduate Research Assistant, Department of Mechanical Engineering. Student Member AIAA.

<sup>&</sup>lt;sup>†</sup>Assistant Professor, Department of Mechanical Engineering. Member AIAA.

Objective properties (e.g., Young's modulus, Poisson's ratio, etc.)

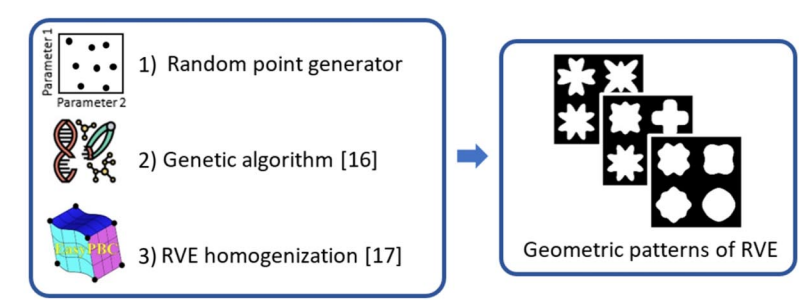


Fig. 1 Schematic for the presented inverse design approach for CMMs [16].

when the low diversity of the populations over several generations appears. With our newly designed search algorithm, the parameter space will be conditionally reduced based on the optimal solutions from the previous runs of the GA to increase global search efficiency. Besides, the works of Maaranen et al. [14,15] indicate that initial populations may significantly influence the optimization results in the GA over several generations. In addition to the pseudorandom numbers applied in a traditional GA, we also study several alternative ways to generate the initial population of the GA within the parameter space. With hundreds of experiments, we can check whether the initial population has significant effects on the best objective function value found for several generations in our design scenarios, including RVEs with periodic and nonperiodic unit cells. The flowchart in Fig. 1 demonstrates the overall procedures of our systematic framework, consisting of 1) alternative point generators for sampling the initial population, 2) a genetic algorithm for searching optimal global results with objective properties, and 3) homogenization methods for estimating the effective properties of the CMMs.

## II. Methodology

## A. Definition of Geometric Patterns

In this study, we choose two-dimensional (2-D) porous cellular solids to demonstrate the inverse design framework for cellular mechanical metamaterials. It is a special but widely used class of CMMs for which the geometric patterns are defined by unit cells within periodically distributed RVEs. The unit cells are characterized by the shape of the pore. The study focuses on the four-fold symmetrical pore, for which the contour is defined as [17]

$$r(\theta) = r_o(1 + \zeta_1 \cos(4\theta) + \zeta_2 \cos(8\theta)) \tag{1}$$

$$r_o = L\sqrt{\frac{2\phi}{\pi(\zeta_1^2 + \zeta_2^2 + 2)}}$$
 (2)

where r is the polar radius;  $\theta$  is the polar angle in  $[0,2]\pi$ ; L is the side length of the unit cell;  $\phi$  is the porosity of the pore shape; and  $\zeta = (\zeta_1, \zeta_2)$  shows the porous parameters, which directly define the family of different pores illustrated in Fig. 2.

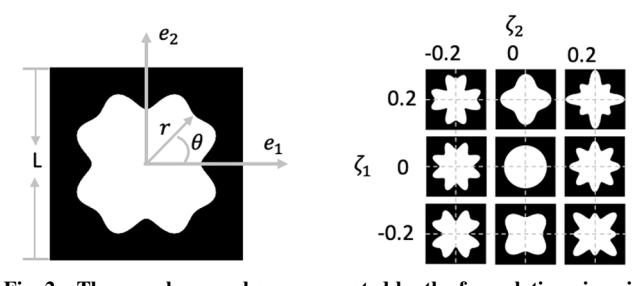


Fig. 2 The sample pore shapes generated by the formulation given in Eqs. (1) and (2).

#### B. Computation of Elastic Properties

To evaluate the linear mechanical properties of 2-D CMMs, this study applies computational homogenization to the RVEs of CMMs using the finite element method. Recently, Omairey et al. [18] developed an plugin of Complete ABAQUS Environment called EasyPBC to determine the homogenized (effective) mechanical properties of user-defined periodic RVEs. The concept of this plugin is similar to the asymptotic homogenization method. It aims to evaluate the effective properties of RVEs by imposing uniform strains on a microscale RVE while ensuring that the deformed external surfaces of the RVE remain periodic [18]. In addition to the computational efficiency and convenience of the commercial finite element software (ABAQUS), this plugin is able to model the composite materials and the materials with void inclusions, hence holding the potential for broader applications in material design [18]. In EasyPBC, the node-to-node periodic boundary conditions (PBCs) are applied at which deformed boundary surfaces can distort and no longer remain plain [18]. Based on the concepts of unified periodic RVE homogenization [19], these PBCs are implemented using linear constraint equations to link nodal degrees of freedom (DOFs) as illustrated in Eq. (3) and Fig. 3 [18]:

$$AxU_{\text{set1}}^{\text{DOF}} + BxU_{\text{set2}}^{\text{DOF}} + CxU_{RP(i)}^{\text{DOF}} = 0$$
 (3)

where A, B, and C are the direction indices (0, -1, and 1); set 1 and set 2 are two opposite or associated sets defined in Fig. 3, U is the nodal displacement of the sets (Fig. 3), DOF are the degrees of freedom that are up to two in the 2-D case, and RP(i) is the reference point that assigns the x and y directions to impose boundary displacements on the RVE and to accommodate ridge body motion. We refer to table 1 in Ref. [18] for assigning the terms in the linear constraint equation.

This study primarily focuses on the two mechanical properties of the effective Young's modulus and the effective Poisson's ratio, which are obtained in postprocessing and determined by Eqs. (4) and (5):

$$E_{11} = \frac{\text{Axial tensile}}{\text{Axial strain}} = \frac{\sum F_{\text{nodal}} / A_{\text{front}}}{\Delta W / W}$$
(4)

$$\nu_{12} = \frac{-\text{Transverse strain}}{\text{Axial strain}} = \frac{\Delta H/H}{\Delta W/W}$$
 (5)

where  $E_{11}$  and  $v_{12}$  are the Young's modulus and Poisson ratio, respectively;  $F_{\text{nodal}}$  is the nodal force in the x and y directions;  $A_{\text{front}}$  is the front surface area that is equal to the height H of the

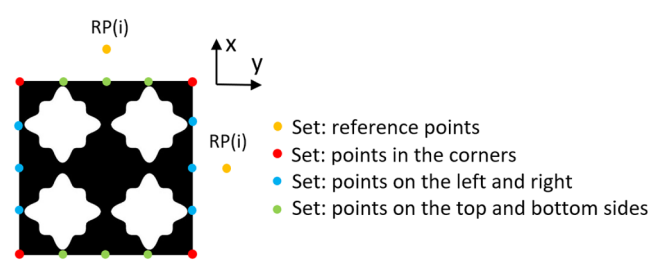


Fig. 3 Classification of node sets on the RVE's boundary.

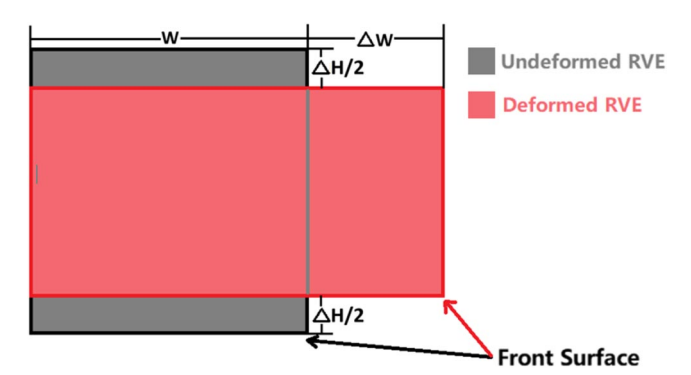


Fig. 4 Deformation of the RVE under tensile strain test.

RVE multiplied by the unit thickness in the 2-D case; and W is the width of the RVE as shown in Fig. 4.

#### C. Optimization Formulation

In this study, the inverse design of microstructured materials can be formulated as a multiobjective optimization problem to minimize the difference between the objective and predicted effective properties of the RVEs. The mathematical formulation of the optimization problem reads as follows:

Minimize 
$$f(\zeta) = [w_1(\nu_{12} - \nu_0)]^2 + [w_2(E_{11} - E_0)]^2$$
  
Find  $\zeta = ([\zeta_1, \zeta_2], \dots, [\zeta_{n-1}, \zeta_n])$   
subject to  $\zeta^L \le \zeta_n \le \zeta^U(n = 1, 2, \dots, 8)$   
 $L_{\text{tolr}} \le \frac{L}{2} - r \sin(\theta), L_{\text{tolr}} \le \frac{L}{2} - r \cos(\theta)$  (6)

where  $\zeta$  denotes the porous parameters;  $w_i$  is a weighted coefficient to scale the two effective properties in the same numerical level; n is the

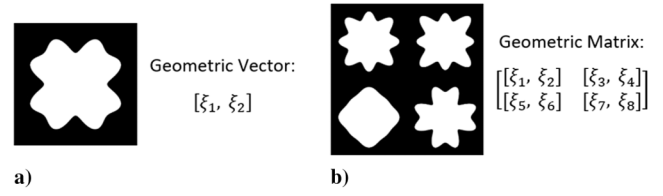


Fig. 5 Baseline geometries of RVEs: a)  $1 \times 1$  RVE and b)  $2 \times 2$  RVE.



Fig. 6 Distance tolerance in the geometric constraint.

number of porous parameters, which is equal to twice as many unit cells within the RVE (see Fig. 5);  $\zeta^L$  and  $\zeta^U$  are the lower and upper bounds of the porous parameters, which are equal to -0.2 and 0.2, respectively; and f is the fitness function of the micro-GA, which is the summation of the absolute errors between the target  $(v_0, E_0)$  and the predicted properties  $(v_{12}, E_{11})$ . The geometric constraint ensures the continuity of structures. It eliminates the convergence issues in the FE simulations when the distance from the edge of the pore shape to the boundary of the unit cell is minimal. Within  $0 \le \theta \le 2\pi$ , the minimum distance should be larger than  $L_{\text{tolr}}$ , as shown in Fig. 6.

#### D. Generation of Initial Population

Following the works of Maaranen et al. [14,15], various random point processes have been studied to understand their impacts on the final objective function values over several generations of the GA. Two inhibition point processes studied in the works of Maaranen et al., which are the simple sequential inhibition process and nonaligned systemic sampling, have a disadvantage in either the computational seed or usability. The simple sequential inhibition process requires a number of trails points to satisfy a predefined distance metric. Besides, nonaligned systemic sampling does not allow users to freely control the sampling size, which is determined by the grid size and dimension of the parameter space. Therefore, considering their efficiency and usability, we will not study the two inhibition processes in this paper. Latin hypercube sampling (LHS) is a simple but efficient approach to distribute the sample points evenly across the parameter space [20]. It can be an alternative random point process to initialize the GA population. It will also be compared to other random point processes studied in the works of Maaranen et al., including a pseudorandom number generator and two quasi-random sequence generators (Sobol and Niederreiter). Overall, our study will explore and compare the effects on the final objective function values using the four different point processes given earlier in this paper, and it will select the best processes for our design scenarios. Figure 7 illustrates examples of the 2-D initial populations with 16 individuals generated using the four random point processes.

## E. Methodology for Microgenetic Algorithm

The structural topological optimization solved by gradient-based methods, such as the standard optimality criteria method [21], requires sensitivity calculations and numerical derivatives. Figure 8 illustrates two contours of the objective function values (in logarithm), corresponding to two different on-demand combinations of the objective properties, in a 2-D parameter space. Because the gradient-based method is dependent on an initial guess [22], the high complexity of the contours in Fig. 8 has a high possibility of failure, such as convergence to an undesired local optimal solution. Besides, the stochastic search algorithms, such as the standard genetic algorithm, are time consuming due to the iterated process of expensive fitness function evaluations [23]. The deep learning method has recently attracted interest in material design applications. It has the ability to learn and model nonlinear and complex relationships, such as geometry-property relations. There is no doubt that a well-trained neural network accelerates the design of materials [24]. However, in

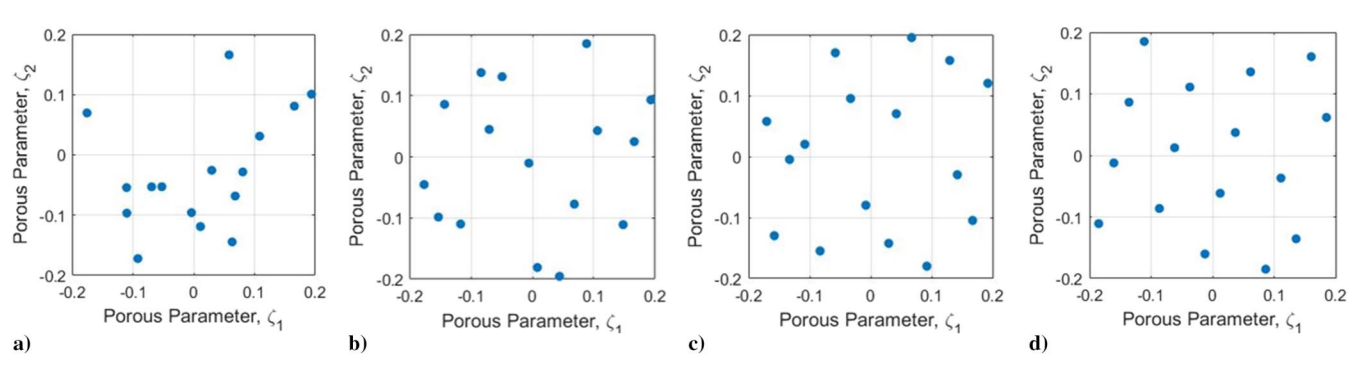


Fig. 7 Sample 2-D initial population generated by a) pseudorandom number generator, b) Sobol sequence generator, c) Niederreiter sequence generator, and d) Latin hypercube sampling.

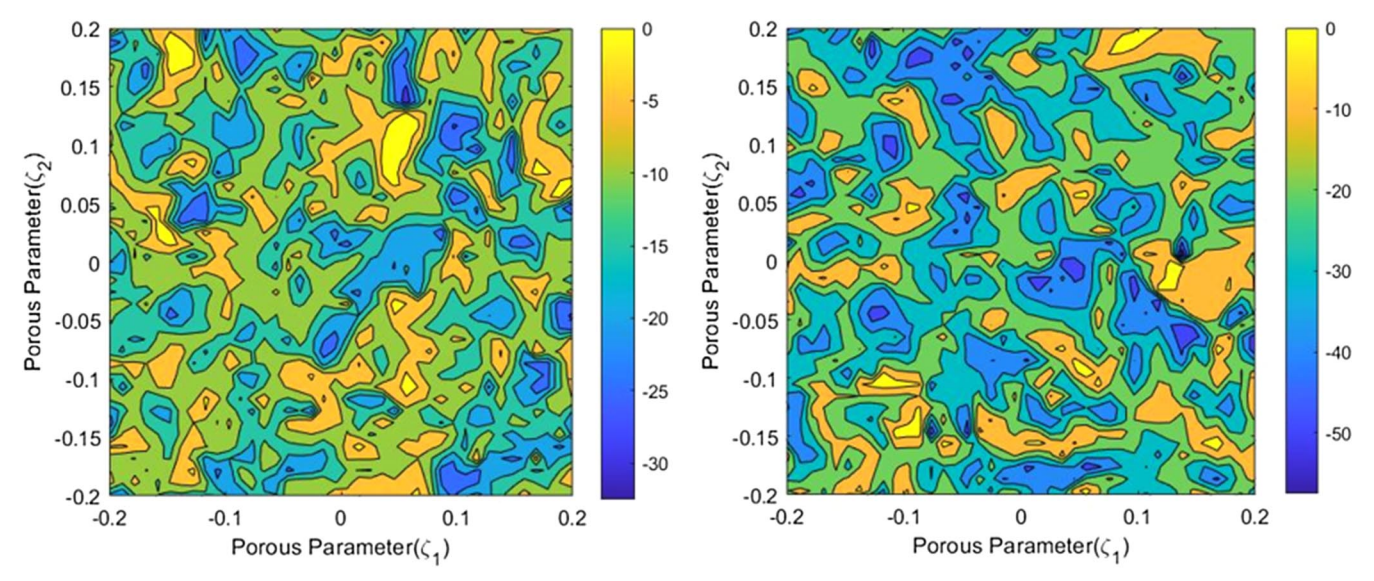


Fig. 8 Contours of the objective function values (in logarithm) with two different combinations of the objective properties in 2-D parameter space.

the meantime, it has the following few drawbacks that need to be considered:

- 1) Building sufficient datasets of geometry–property relations and training neural networks are exhaustive processes.
- 2) Coverage of the material property predictions is not guaranteed by the limited range of datasets, and thus the fidelity of NNs is affected.
- 3) Achieving the desired RVE geometry that provides the objective properties cannot be guaranteed due to the discontinuities in the prediction ranges.
- 4) Interpretability of the predictions is limited due to the implicit link between the inputs and outputs.

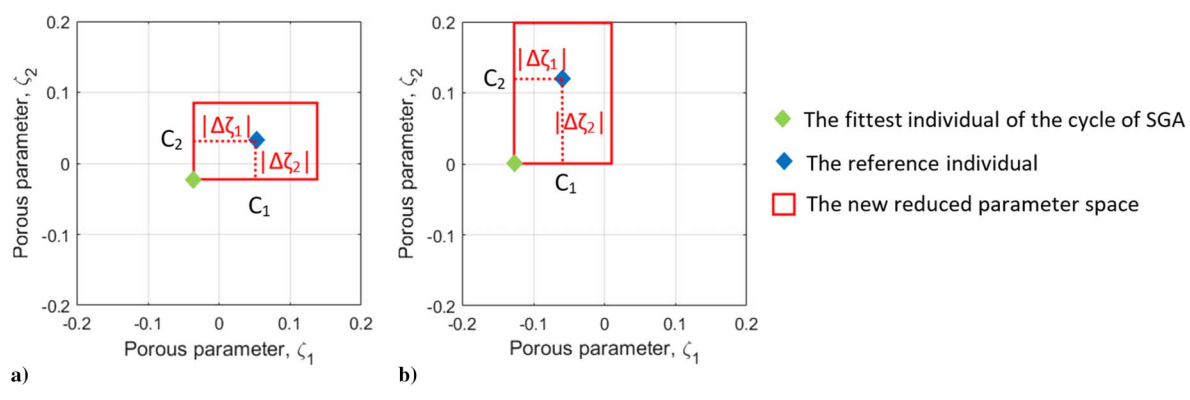
Here, we propose an experience-free and heuristic searching strategy based on a microgenetic algorithm ( $\mu$ GA) to address the preceding issues. Without a database, our method has the capability to discover the complex nonlinear relationships between the geometries of RVEs and their corresponding properties by evolutionary algorithms. Considering the computational expense of the standard genetic algorithm (SGA), we employ  $\mu$ GA, which undergoes SGA operators including tournament selection, crossover, uniform mutation, and elitism but requires a small population size in each cycle. Obviously, with a small population size, the SGA has difficulty maintaining diversity over several generations. Moreover, it could induce premature convergence due to the presence of a local optimum solution. To avoid this problem, the basic idea of  $\mu$ GA is to restart the SGA with a small population size (N) in multiple cycles. Once the diversity of the current cycle is low, the fittest individual is kept as a reference individual and N-1 new individuals from the initial population are introduced to the next cycle of the SGA. Meanwhile, the range of the parameter space remains the same. The diversity of the generations in the  $\mu$ GA is evaluated by the overall change of fitness values among the stall generation limits. The basic idea allows the  $\mu GA$  to continuously search for global optimum solutions and avoid the current searching step trapping in the local minima of our optimization problem.

In the  $\mu$ GA, the searching strategy continuously processes a new cycle of the SGA while introducing the new fittest individual until the maximum iteration number or error tolerance is reached, where the error tolerance is the maximum relative error between the objective and optimal properties. The fittest individual in the early stages of the searching process may already have outstanding values of the objective (fitness) function, but it may not satisfy the error tolerance of the stopping criteria. Less strict stopping criteria of the successive cycles, such as large maximum iteration number and large function tolerance, induce the increase in the total number of generations of the SGA. It might allow the iterative search process of the SGA has the possibility to optimize the current fittest individual approaching the objective value due to the large generation number. With the

restart of the SGA sufficient times, the iterated search process has the possibility to optimize the current fittest individual approaching the objective value. However, for a large number of restarts in the SGA, the iterated search process is time consuming, even with the small population size. Here, we assume that the current fittest individuals (local minima) achieved in the case of no improvement in the optimum solution over several cycles have a significant possibility of being located near the global minima. The assumption was proved by the experiments with RVEs containing one periodic unit cell (Fig. 5a). In the parameter space, we evaluated the Euclidean distances between 50 local minima (determined by 50 runs of the SGA) and global minima, which were defined by a known geometric pattern of RVEs with corresponding homogenized properties. Table 1 shows 10 identical global minima with the average distance of their 50 local minima. In Table 1, the average distances for all the cases are less than 50% of the width of the parameter space of 0.4, which is determined based on the predefined range of porous parameters from -0.2 to 0.2 in Sec. II.C. The average distance in case 4 even reaches 4% of the width. Inspired by the results, we can reduce the parameter space based on the current fittest individuals of the SGA to decrease the computational cost. Considering a more complex design scenario, like the one with a higher-dimensional parameter space and a Pareto optimal set, a new parameter space cannot simply be reduced based on a single local minimum and a specifically designated width. The SGA with a new reduced space should be determined by referring to at least two local minima, which allows us to obtain the new fittest individuals with extremely high accuracy that satisfy the error tolerance to stop the searching process. The statement is validated by the results in Sec. IV.C.

Table 1 Summary of Euclidean distances between local minima and one global minimum

Example index	Global minima	Corresponding properties $[\nu_0, E_0]$	Average Euclidean distance of 50 local minima
1	[0.1800 -0.1367]	[0.1843 1111.87 MPa]	0.1393
2	[-0.1435 0.0048]	[0.1939 1417.06 MPa]	0.0527
3	[0.0885 0.1715]	[0.1571 994.75 MPa]	0.0772
4	[0.0928 0.0999]	[0.1853 1137.40 MPa]	0.0765
5	[-0.0371 - 0.1042]	[0.2020 1289.35 MPa]	0.0481
6	[0.1370 0.0652]	[0.1896 1107.50 MPa]	0.1165
7	[0.1011 - 0.0013]	[0.2095 1274.87 MPa]	0.0248
8	[0.0188 - 0.0388]	[0.2152 1372.35 MPa]	0.0174
9	$[-0.1572\ 0.0897]$	[0.1680 1357.84 MPa]	0.0278
10	[-0.1060 -0.0404]	[0.2049 1393.67 MPa]	0.0288



Construction of the new reduced parameter space.

Therefore, the new range of the n-dimensional parameter space is determined based on the current fittest individual (the first local minimum) with  $[\zeta_{1,0}, \zeta_{2,0}, \dots \zeta_{n,0}]$  and the new fittest individual (the second local minimum) with  $[\zeta_{1,1}, \zeta_{2,1}, \ldots, \zeta_{n,1}]$ , achieving by running a new cycle of the SGA without any reference individuals in the initial population. The width of the new n-dimensional parameter space is determined as twice the absolute difference of the porous parameters in each dimension,  $2 \times |\zeta_{n,0} - \zeta_{n,1}|$ , as demonstrated as Fig. 9. Once the side lengths of a reduced parameter space  $C_i$  in each dimension are determined, the new cycle of the SGA will be processed without any reference individual in the initial population. The fittest individual in the new cycle can be continuously optimized by following the basic idea of the  $\mu$ GA in the reduced parameter space. The following pseudocode illustrates the detailed procedure of our global searching strategy:

```
function micro-GA
  begin
```

Define porous parameters  $\zeta \in [\zeta_{0,\min}, \zeta_{0,\max}]$  and the number of cycles of SGA(i) = 0.

Case 1: 1) Initialize the population P with size N.

- 2) Optimize the initial population by the SGA.
- 3) Save the fittest individual  $K_{best}$  and its objective
- function value  $f_{best}$ .

4) i = i + 1.

while  $f_{\text{best}} > \text{tolerance or } i \le \text{maximum iteration}$ , then Case 2: 1) Introduce  $K_{best}$  and initialize P with N-1.

- 2) Optimize the initial population by the SGA.
  - 3) Save the fittest individual  $K_{best}$  and its objective

function value  $f_{\it best}$ .

4) i = i + 1.

if  $f_{\text{best}} \leq \text{tolerance } or i > \text{maximum iteration}, then$ end function

else

repeat

begin

Run case 2.

if  $f_{\text{best}} \leq \text{tolerance } or \ i > \text{maximum iteration, } then$ end function

**until**  $f_{\text{best}}$  of the current cycle of SGA =  $f_{\text{best}}$  of the previous cycle of the SGA

Save  $f_{\text{best}}$  of the current cycle  $f_{0,\text{best}}$  with  $[\zeta_{1,0}, \zeta_{2,0}, \dots \zeta_{N,0}]$ 

Save  $f_{\text{best}}$  of the new cycle of the SGA  $f_{0,\text{best}}$  with  $[\zeta_{1,1}, \zeta_{2,1},$  $\ldots \zeta_{N,1}$ ].

Case 3: 1) Define new range of  $\zeta_N$  in N dimensions

while  $j \leq N$ Determine absolute difference between  $\zeta_{i,0}$  and

 $\zeta_{j,1}$  in jth dimension,  $\Delta \zeta_j = |\zeta_{j,0} - \zeta_{j,1}|$ .  $if \zeta_{j,1} + \Delta \zeta_j \ge \zeta_{0,\max}$   $\zeta_{j,\max} = \zeta_{0,\max}$ 

```
\zeta_{j,	ext{max}} = \zeta_{j,1} + \Delta \zeta_{j}
end

\mathbf{if} \zeta_{j,1} - \Delta \zeta_j \le \zeta_{0,\min} 

\zeta_{j,\min} = \zeta_{0,\min}

                                    \zeta_{j, \min} = \zeta_{j, 1} - \Delta \zeta_{j}
end
                           end
                             2) Run case 1 with a new parameter space defined by
                            3) Save the fittest individual K_{\mathrm{best}} and its objective
function value f_{\text{best}}.
                             5) if f_{\text{best}} \leq \text{tolerance } or i > \text{maximum iteration}, then
```

end function else repeat begin Run case 2. i = i + 1. *until*  $f_{\text{best}} \leq \text{tolerance } or i > \text{maximum iteration}$ 

end function.

## III. Numerical Examples and Results

## A. Preliminary Settings

In this section, the effectiveness of the inverse design method is demonstrated by testing two numerical examples: RVEs with periodic unit cells, and RVEs with nonperiodic unit cells. The parametrization describes the unit cells of the RVEs in Eqs. (1) and (2). In the first numerical example (2-D study case), the geometric patterns of the RVEs consist of  $1 \times 1$  periodical unit cells, which are defined by the  $1 \times 2$  geometric vector  $[\zeta_1, \zeta_2]$  shown in Fig. 5a. The second numerical example [eight-dimensional (8-D) study case] has RVEs consisting of  $2 \times 2$  nonperiodic unit cells, for which the geometric patterns are defined by the  $2 \times 4$  geometric matrix  $([\zeta_1,\zeta_2][\zeta_3,\zeta_4];[\zeta_5,\zeta_6][\zeta_7,\zeta_8])$  shown in Fig. 5b. The chosen sizes of the RVEs in the two numerical examples are large enough to represent the microstructure without introducing nonexisting properties [25], and they are small enough to reduce the computational expense in finite element analysis. In our study, the RVEs in the two numerical examples are assigned to an isotopic and linear elastic material called unfilled polyetherimide (Young's modulus = 3580 MPa, and Poisson's ratio = 0.35 [26]). The range of porous parameters  $\zeta$  is identical in each dimension, from -0.2 to 0.2. The size of the unit cell is defined by the side length of L=10 mm. The smallest distance  $L_{\rm tolr}$  between the edge of the pore shape and the boundary of the unit cell is designated as 0.5 mm. The porosity of the unit cells  $\phi$  is equal to 0.4. Besides, the optimization problem in this section is solved using the  $\mu$ GA with the same mutation rate of 0.1, a crossover rate of 0.8, a population size of 16,

and a stall generation limit of 32. In the inner loops of our searching methodology, all cycles of the SGA have the same stopping criteria:

- 1) The change of the optimal value of the fitness function during restarting of the micro-GA should be less than 1e-4.
- 2) The maximum iteration number should be smaller than 50. In addition, there are two stopping criteria for the outer loops of our searching methodology:
  - 1) the maximum number of cycles should be less than 10.
- 2) The final optimal properties should satisfy a certain relative error between the objective and optimal properties.

The two objective properties for this study were chosen to be the effective Young's modulus of the CMMs and its effective Poisson's ratio. In addition, we intend to select combinations of objective properties that cover the design spaces of the 2-D and 8-D study cases, and meanwhile ensure the diversity of the expected geometric patterns of the RVEs, which have various curvatures of the porous surfaces in the unit cells. The following numerical examples demonstrate that the presented approach successfully identified all these different geometries while optimizing the geometric patterns with preferred combinations of the two effective properties.

## B. RVEs with Periodic Unit Cells

Suppose a geometric pattern of the  $1 \times 1$  RVE with the periodic unit cell is desired that exhibits an objective effective Young's modulus as well as Poisson's ratio. It corresponds to a 2-D study case with two design parameters  $[\zeta_1, \zeta_2]$ . In the 2-D study case, the tolerance of the relative error with respect to the objective properties is defined as 0.05% in comparison to the objective properties. In the beginning of our optimization framework, there is no prior information about the local or global minima available for initializing the population of the SGA. Therefore, uniformly distributed sample points with diverse values and locations might be useful for searching optimum solutions throughout the 2-D parameter space [15]. Traditionally, the initial population of the SGA is generated by a pseudorandom number generator (PRNG) [14]. Our study compares its effect on the objective function values to three alternative random point generators, including the Sobol sequence generator (SSG), the Niederreiter sequence generator (NSG), and Latin hypercube sampling. The empirical empty space statistics (ESS) function evaluates their goodness for the uniform distribution property, which is defined as [14]

$$ESS(r) = 1 - Pr(B(x, r) \text{ is empty})$$
 (7)

where x is a randomly chosen point in the feasible region, B(x, r) is a ball centered at x with radius r, and Pr denotes the probability [14]. The function randomly assigned the ball B with the radius r at the center x in the feasible region. Then, the probability of the function is the likelihood of having no sample points in the ball B. Figure 10a illustrates the relationship between the radius of the ball B and the average ESS function values of hundreds of point generations. As the radius increases, the ball B is less likely to be empty, leading to an increase in the ESS function. If the emptiness of the ball B is more sensitive to the change of radius and depends less on its center x, the curve tends to be steep. In other words, the generator with more evenly

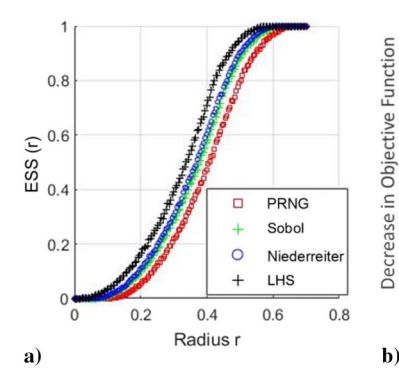
distributed sample points within the parameter space has a steeper curve of the ESS function. Hence, the sequence from the highest to the lowest in the uniformity of the sample distribution is LHS, NSG, SSG, and PRNG, respectively. In Fig. 10a, LHS first converges to the maximum value of the ESS function, representing that it has the highest uniformity among the four generators.

In addition to the uniformity, we check the accuracy of the four random point generators. The accuracy is evaluated by solving the optimization problem with 20 different objective properties, shown in Table 2. Due to the minimization problem, the smaller the objective function value is, the higher the accuracy of the optimum solution accuracy is. We solve each problem with four variants of the SGA 100 times. The benchmark results in Fig. 10b are the objective function values obtained with the PRNG. The heights of the bars in Fig. 10b represent the decrease in the objective function values as compared to the benchmark. Table 2 summarizes the results from Fig. 10b, including the average decrease in the objective function values in percentage, the number of improved objective function values, and the variance of the decreases in the objective function values in the percentage of all tested objective properties. Generally, the objective function values can be successfully improved by replacing any of the three alternative generators with the benchmark. Although LHS reduces a large number of objective function values in percentage, its performance or stability varies considerably from case to case by referring to the relatively large values of the variance in Table 2. The overall results from Fig. 10b and Table 2 prove that the distributions of the initial population have an important effect on the objective function values in the 2-D case. However, the comparison of the variance in Table 2 indicates that the highest uniformity of the initial population does not necessarily contribute to the best performance in optimizing the geometric patterns of the RVEs. Overall, based on the comprehensive evaluations from Table 2, we choose either the NSG or the SSG as the random point generator of the SGA in our searching strategy.

After evaluating the four random point generators, we process our complete searching strategy with a quasi-random point generator, such as the SSG, to solve the optimization problem with 20 different objective properties, shown in Table 3. Table 3 numerically summarizes the optimization results, including the objective properties, the order of the SGA cases from the pseudocode in Sec. II.E, the relative errors in percentage as compared to the objective properties, and the total number of generations in the SGA. Owing to the benefits of the quasi-random point sampling, the objective properties in the several examples can be achieved only in a single cycle, shown in examples

Table 2 Summary of results from Fig. 10b (2-D)

Random point generator	Average decrease in objective function, %	Number of the improved objective function	Variance in objective function
SSG	65.32	16	0.8878
NSG	63.55	17	0.7621
LHS	114.97	14	5.6341



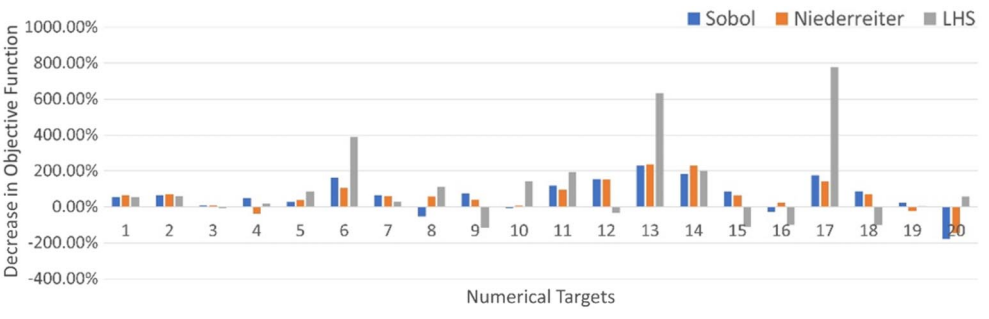


Fig. 10 Comparison of the four random point generators in 2-D parameter space: a) ESS function vs radius, and b) decrease in objective function values.

Table 3 Summary of the optimization results (2-D)

		Order of	•	
Example	J _ I _ I	SGA	Relative error	Total number
index	$[\nu_0, E_0]$	cases	$[\%\nu,\%E]$	of generations
1	[0.1755, 1068.33 MPa]	12	[0.010%, 0.037%]	] 84
2	[0.1968, 1442.13 MPa]	122	[0.045%, 0.027%]	] 108
3	[0.2171, 1408.04 MPa]	1213	[0.002%, 0.011%]	] 111
4	[0.2059, 1251.02 MPa]	121	[0.020%, 0.015%]	] 134
5	[0.2120, 1378.09 MPa]	1	[0.004%, 0.001%]	] 32
6	[0.1932, 1401.69 MPa]	1	[0.033%, 0.008%]	] 47
7	[0.2175, 1349.87 MPa]	12	[0.002%, 0.012%]	] 78
8	[0.1917, 1240.80 MPa]	12213	[0.001%, 0.000%]	] 186
9	[0.1838, 1069.64 MPa]	121	[0.010%, 0.007%]	] 81
10	[0.2116, 1440.36 MPa]	12132	[0.002%, 0.033%]	] 160
11	[0.1731, 1363.41 MPa]	1221	[0.000%, 0.000%]	] 128
12	[0.2077, 1431.43 MPa]	12	[0.001%, 0.000%]	] 38
13	[0.2077, 1326.66 MPa]	12132	[0.005%, 0.050%]	] 177
14	[0.1591, 1273.32 MPa]	12132	[0.002%, 0.000%]	] 185
15	[0.1845, 1110.27 MPa]	121	[0.002%, 0.000%]	] 92
16	[0.1910, 1129.32 MPa]	1	[0.000%, 0.000%]	] 35
17	[0.1857, 1180.21 MPa]	122	[0.037%, 0.033%]	] 104
18	[0.1522, 1184.82 MPa]	121	[0.000%, 0.000%]	] 87
19	[0.1731, 1189.14 MPa]	1	[0.000%, 0.000%]	] 45
20	[0.1866, 1140.06 MPa]	121	[0.000%, 0.000%	] 86

5, 6, 16, and 19. Figure 11 visually demonstrates the collective converging histories of all cycles of the SGA within the whole process of the  $\mu$ GA. The history shows the logarithm of the objective function values over the generations (iteration steps). In Fig. 11, the solid vertical lines split the history into several sections, representing a cycle of the SGA and denoted with the corresponding case index from the pseudocode. Some of the example problems in Table 3 (such as examples 1, 2, 7, 12, and 17) can be directly solved by the basic idea of the  $\mu$ GA combined with cases 1 and 2 from the pseudocode. Some of the example problems (such as examples 4, 9, 11, 15, 18, and 20) require restarting the SGA without any reference individual after the several cycles. Some other example problems (such as examples

3, 8, 10, 13, and 14) require reducing the initial parameter space to improve the fittest individual further, which is stuck at the local optimum using case 1, case 3, and case 2 if necessary. Thus, the results shown in Table 3 and Fig. 11 numerically and visually prove the effectiveness of our searching strategy, respectively.

## C. RVEs with Nonperiodic Unit Cells

Suppose a geometric pattern of the  $2 \times 2$  RVE with the nonperiodic unit cell is desired that exhibits the objective effective Young's modulus and Poisson's ratio. It is a 2-D study case with eight design parameters  $[\zeta_1, \zeta_2, \zeta_3, \zeta_4, \zeta_5, \zeta_6, \zeta_7, \zeta_8]$ . Because the higher complexity results in more significant variances in material properties, we set the tolerance of the relative error in the 8-D study case as 0.01% to increase the reliability of our optimum results. Before processing our searching strategy within the optimization problem, we first evaluate the uniformity of the four random point generators by the ESS function in Fig. 12a. The population size of the SGA is assigned as 16, which is the same as the 2-D study case. In Fig. 12a, we find that the converging behaviors of the four random point generators are very similar, and their converging history plots are almost overlapping. These results are caused by the small population size chosen in the high-dimensional parameter space. Consequently, the changes in the random point generators in the SGA slightly affect the initial population's point distribution; thus, their uniformity is nearly identical. Moreover, by processing a single cycle of the SGA with 20 different objective properties, we determine whether the sample distribution affects the accuracy of the objective function values in the high-dimensional study case. Table 4 summarizes the results from Fig. 12b and shows that the four random point generators have similar performances in optimizing the geometric patterns of the RVEs. Therefore, we conclude that, in our case scenario, changing the random point generators hardly influences the objective function values of the SGA with a small population size and a large number of design parameters. Therefore, we could choose any of the four random point generators to process our searching strategy in this study case.

The next step is to perform our complete searching strategy to solve the optimization with 20 different objective properties, shown

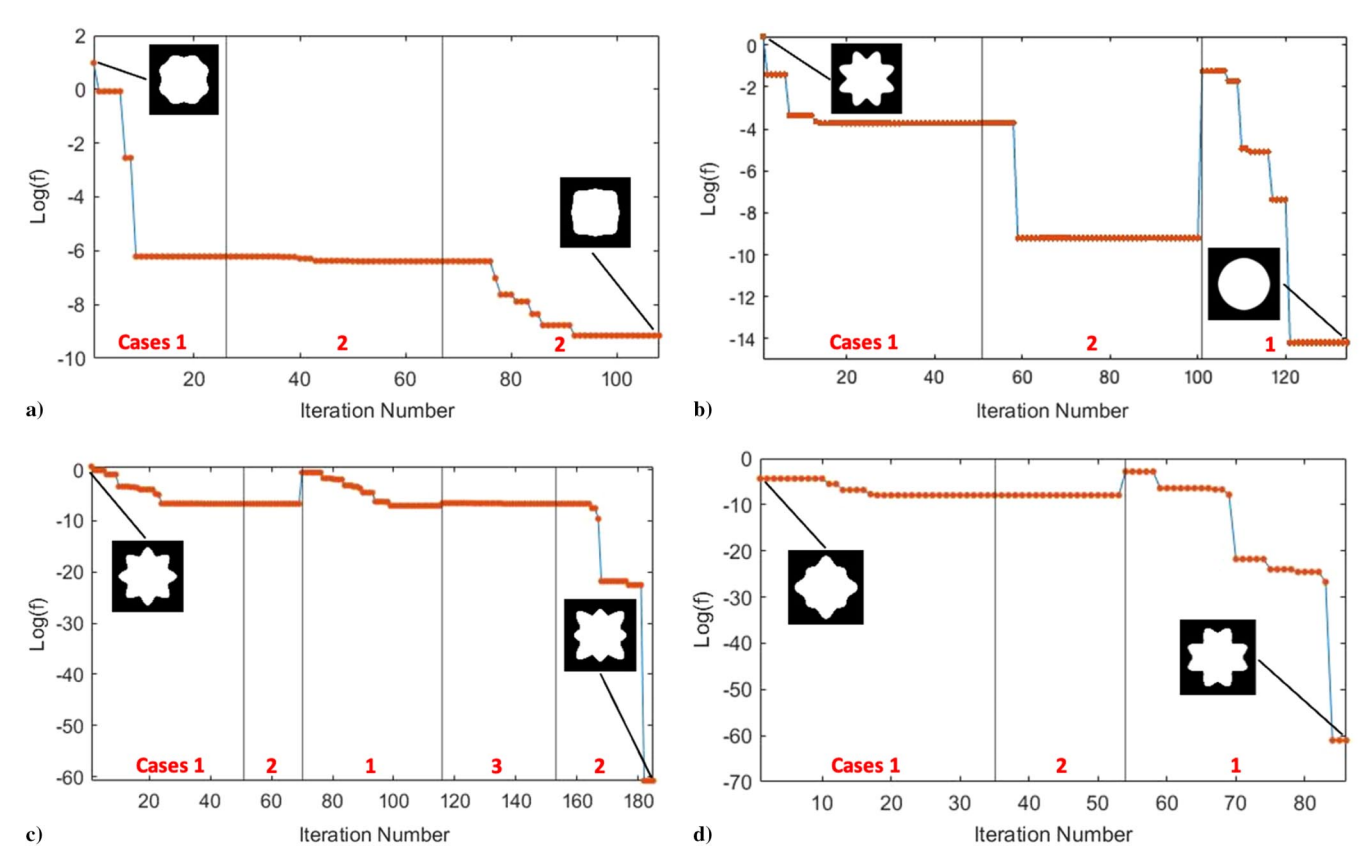


Fig. 11 Combined converging history of four sample examples in Table 3: a) example 2, b) example 4, c) example 14, and d) example 20.

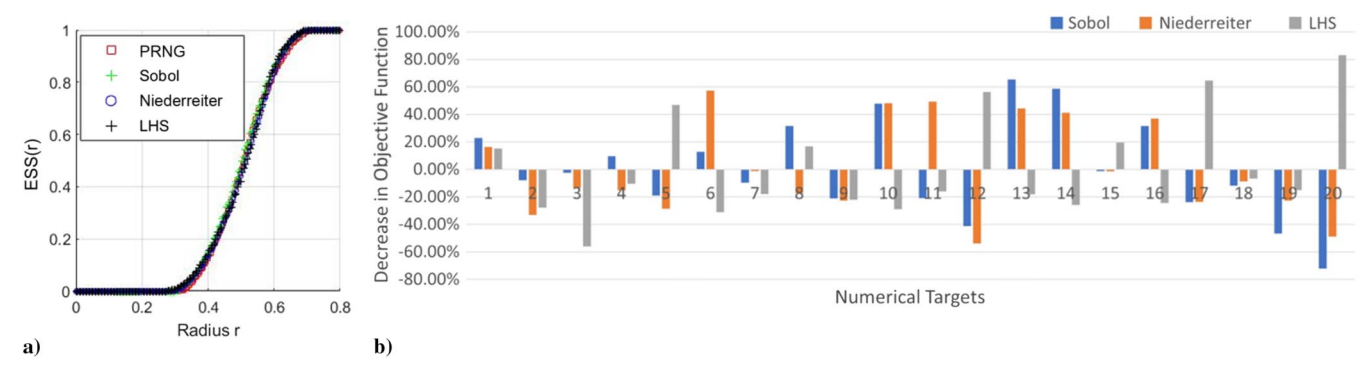


Fig. 12 Comparison of the four random point generators in 8-D parameter space: a) ESS function vs radius, and b) decrease in objective function values.

Table 4 Summary of results from Fig. 12b (8-D)

Random point generator	Average decrease in objective function, %	Number of the improved objective function	Variance in objective function
SSG	0.16	8	0.1261
NSG	0.20	7	0.1546
LHS	0.18	7	0.1372

in Table 4. Like Table 2, the optimization results are summarized in Table 4, including the objective properties, the order of the SGA cases from the pseudocode in Sec. II.E, the percentage errors as compared to the objective properties, and the total number of generations in the SGA. The growth of the complexities of the geometric patterns of the RVEs provides sufficient freedom to design the microstructures of the CMMs. It results in the possibility that the RVEs with different geometric patterns share nearly identical effective properties. With a limited amount of candidate solutions, it is not difficult for the SGA in an 8-D study case to achieve optimal solutions with a small error. This is shown by the results of examples 4, 7, 8, 11, 19, and 20. Even without the updated method to generate the initial population, the increased freedom for material design allows these examples to achieve satisfactory results within a single cycle. Some of the example problems in Table 5 (such as examples 1, 10, 14, 15, 16, and 18) can continuously reduce the objective function values simply through the basic idea of the  $\mu$ GA combined with cases 1 and 2 from the pseudocode. Some of the example problems (such as examples 5, 9, and 13) require dealing with premature convergence by neglecting

Table 5 Summary of the optimization results (8-D)

		<sub>1</sub>		(= -)
Example	Objective properties $[\nu_0, E_0]$	Order of SGA cases	Error [%ν, % <i>E</i> ]	Total number of generations
1	[0.1965, 1203.59 MPa]	122	[0.000%, 0.000%]	
2	[0.1802, 1217.30 MPa]	12132	[0.007%, 0.001%]	•
3	[0.1902, 1181.81 MPa]	122132	[0.004%, 0.010%]	•
4	[0.1684, 1149.97 MPa]	1	[0.001%, 0.007%]	•
5	[0.1838, 1282.16 MPa]	121	[0.006%, 0.003%]	117
6	[0.1783, 1175.81 MPa]	12132	[0.001%, 0.008%]	171
7	[0.1891, 1151.91 MPa]	1	[0.008%, 0.008%]	36
8	[0.1817, 1094.37 MPa]	1	[0.005%, 0.001%]	54
9	[0.1470, 1062.27 MPa]	1221	[0.006%, 0.007%]	] 140
10	[0.1504, 1144.93 MPa]	122	[0.001%, 0.010%]	101
11	[0.1606, 1101.14 MPa]	1	[0.002%, 0.010%]	47
12	[0.1670, 1235.14 MPa]	122131	[0.007%, 0.005%]	201
13	[0.1826, 1372.53 MPa]	1221	[0.004%, 0.008%]	139
14	[0.1954, 1293.73 MPa]	12	[0.001%, 0.007%]	92
15	[0.2031, 1169.70 MPa]	1222	[0.007%, 0.003%]	141
16	[0.2088, 1212.85 MPa]	12	[0.007%, 0.006%]	74
17	[0.2187, 1119.45 MPa]	12132	[0.007%, 0.007%]	•
18	[0.2031, 1073.87 MPa]	12222	[0.002%, 0.004%]	
19	[0.1882, 1028.95 MPa]	1	[0.003%, 0.002%]	
20	[0.1845, 1165.72 MPa]	1	[0.008%, 0.006%]	1 44

the results from previous cycles instead of starting a new SGA without any reference individual. Some other example problems (such as examples 2, 3, 6, 12, and 17) have the fittest individual, which is stuck at the local optimum over several cycles of the SGA. Reducing the initial parameter space allows the problem to improve the individual further using case 1, case 3, and case 2 if necessary. Moreover, the collective converging histories in Fig. 13 demonstrate the optimization process over several cycles of the SGA in a straightforward way. The histories clearly illustrate the issue of premature convergence, the restarts of the SGA for a new fitness individual, and the continuous decrease in the objective function values. Overall, both the numerical and visual results in the 8-D study case indicate the effectiveness of our searching strategy.

#### IV. Discussion

The results from the numerical examples demonstrate the effectiveness and reliability of our proposed inverse design method. In this section, we further illustrate the motivations for employing the microgenetic algorithm with the new searching strategy instead of the traditional/standard genetic algorithm. To make comparisons of the two optimization methods, we set up one control group with the  $\mu$ GA and two experimental groups with the SGA. All test runs were performed on a laptop computer with a 2.60 Hz Intel Core i7-10750H processor and 16 GB DDR4 (Double Data Rate Fourth Generation) memory at 2133 MHz. All groups intend to solve the same inverse design problem with 20 objective properties from the previous section for 2-D and 8-D numerical cases. We define the control group as the same tests processed in Sec. III and directly refer to Table 3 (2-D) and Table 5 (8-D) as the control group's results. In the experimental group, every setting of the GA and the choice of the random point generators are the same as in Sec. III, except for the population size and the stopping criteria. The first experimental group maintains a population size of 16. The second experimental group doubles the population size from 16 to 32 in the 2-D study case and quadruples the size from 16 to 64 in the 8-D study case. Meanwhile, we appropriately adjust the stopping criteria for all the experimental groups, such as the maximum iteration number and the default fitness tolerance. It aims to avoid the optimization process stopping early with unsatisfactory results caused by the relatively strict stopping criteria in Sec. III. Besides, all study cases have the same error tolerance defined in Sec. III. The errors in the 2-D case have an error tolerance, for which both the Young's modulus and Poisson's ratio should be less than 0.05%. In the 8-D case, the errors should be less than 0.01%. The following tables summarize the comparison results between the control and experimental groups, containing the population size, the stopping criteria, the average error between the optimal and objective properties in percentage, the number of optimal results satisfying the error tolerances, and the average running time in hours. All table results are achieved by solving the 20 inverse design problems in Tables 3 and 5 for 2Dand 8D-study cases, respectively.

In Tables 6 and 7, the first experimental group, with the same population size and the relatively lenient stopping criteria as compared to the control group, is unable to achieve the optimal solutions

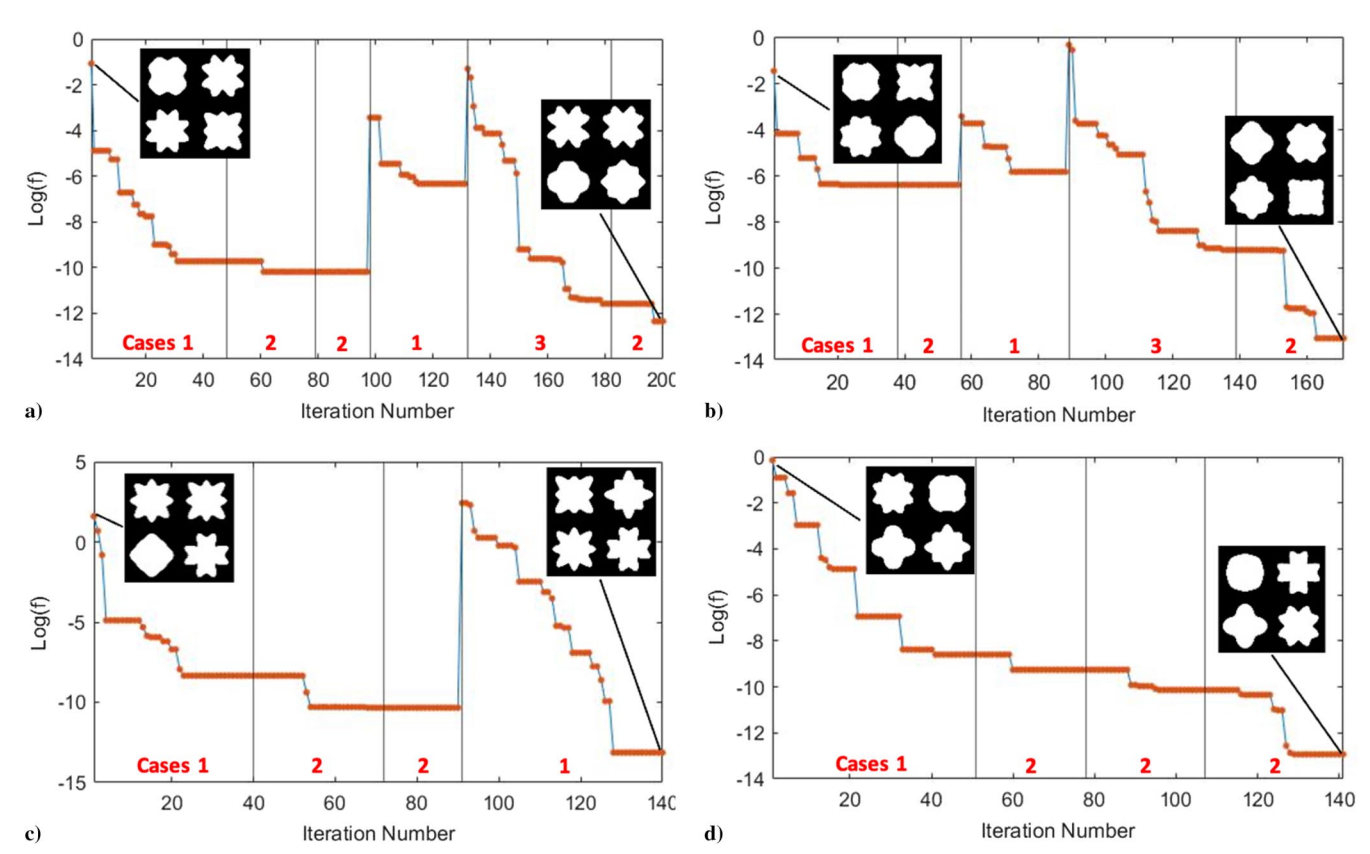


Fig. 13 Combined converging history of four sample examples in Table 5: a) example 3, b) example 5, c) example 9, and d) example 15.

 Table 6
 Comparison of results between the control group and the first experimental group (2-D)

Group	Population size	Maximum iteration number	Fitness tolerance	Average error $[\%\overline{\nu}, \%\overline{E}]$	Counts (satisfied)	Average time, h
Control	16	50	1e-5	[0.009%, 0.012%]	20	2.49
Experimental 1	16	50	1e-5	[0.389%, 0.334%]	6	1.74

Table 7 Comparison of results between the control group and the first experimental group (8-D)

Group	Population size	Maximum iteration number	Fitness tolerance	Average error $[\%\overline{\nu}, \%\overline{E}]$	Counts (satisfied)	Average time, h
Control	16	50	1e-5	[0.004%, 0.006%]	20	2.86
Experimental 1	16	50	1e-5	[0.093%, 0.084%]	3	2.19

that satisfy the error tolerance defined in Sec. III. Then, we double the population size in the 2-D case and even quadruple the population size in the 8-D case. The increases in the population size cause the increased amount of candidate solutions in a single cycle of the SGA, leading to a large possibility of achieving feasible individuals. In Tables 8 and 9, the large population size is found to improve the accuracy in the optimal solutions of the SGA. In both 2-D and 8-D

cases, the number of counts in the feasible solutions is increased. Moreover, both cases demonstrate a certain level of improvement in the average errors; however, they still do not satisfy the tolerance. Nevertheless, this improvement causes a substantial growth in the computational expense.

Thus, our proposed inverse design framework has the capability to obtain the optimal solution with high accuracy while maintaining

Table 8 Comparison of results between the control group and the first experimental group in 2-D

Group	Population size	Maximum iteration number	Fitness tolerance	Average error $[\%\overline{\nu}, \%\overline{E}]$	Counts (satisfied)	Average time, h
Control	16	50	1e-5	[0.009%, 0.012%]	20	2.49
Experimental 2	32	100	1e-7	[0.069%, 0.131%]	12	3.42

Table 9 Comparison of results between the control group and the first experimental group in 8-D

Group	Population size	Maximum iteration number	Fitness tolerance	Average error $[\%\overline{\nu}, \%\overline{E}]$	Counts (satisfied)	Average time, h
Control	16	50	1e-5	[0.004%, 0.006%]	20	2.86
Experimental 2	64	300	1e-7	[0.004%, 0.011%]	13	16.9

outstanding computational efficiency in solving the inverse design problem with a few objective properties. For a large number of objective properties, a well-trained neural network definitely has a considerable advantage in computational efficiency over our method. On the other hand, the users of our approach do not need to build an extensive database of NNs that can exhaust computational resources. During the training process of the NN, the lack of data limits the design space of the materials while reducing the accuracy of the predicted results. Moreover, we solve the inverse design problem over physically explainable optimization in the geometric patterns of the RVEs. There is no guarantee that the properties of the CMMs are smoothly distributed in the material property closure. Therefore, it questions the reliability of regression in deep learning. In a neural network, the implicit connections between the input and output layers hinder its versatility and scalability. Instead, our proposed method can deal with different material types by directly modifying the underlying physics-based model in our programming.

#### V. Conclusions

This paper developed an experience-free and systemic methodology for exploring the parameter space of cellular mechanical metamaterials using the multiobjective genetic algorithm. It opens new avenues to harness genetic algorithms to realize user-defined properties. The method adopts the representative volume element homogenization method for the multiscale material system to predict its effective properties in ABAQUS. The homogenization method is not only compatible with isotropic materials but also with anisotropic composite materials. The broad application of the homogenization method provides possible future research as an extension of the current work. In addition, the geometric patterns of the RVEs are evolved using the new searching strategy based on the microgenetic algorithm. The current experimental results illustrate that the strategy avoids premature convergence in solving an inverse design problem using the  $\mu$ GA, and it maintains high accuracy in optimal results while requiring no prior information about the pattern-property pairs. In the meantime, as compared to the standard exhaustive genetic algorithm, it achieves relatively low computational expense with the small population size and the conditionally reduced parameter space. Moreover, this study examines four different random point generators in the standard genetic algorithm. In a high-dimensional parameter space, the small population size minimizes the impact on the objective function values with any alternative generators mentioned in this paper. Besides, owing to the GA's capability of imitating the natural evolution, the proposed method can easily be applied to the inverse design of other cellular metamaterials with highdimensional discrete design parameters, such as trusslike structures and other cellular metamaterials where the geometric patterns of RVEs are defined by an ensemble of binary values (genes).

## Acknowledgments

This research was supported by NSF CMMI (National Science Foundation in Civil, Mechanical and Manufacturing Innovation) Division grant (CMMI-2053840). The authors would like to acknowledge the assistance provided by Sadik Omairey in sharing the interface plugin of Complete ABAQUS Environment (EasyPBC).

#### References

- [1] Hu, Z., Thiyagarajan, K., Bhusal, A., Letcher, T., Fan, Q. H., Liu, Q., and Salem, D., "Design of Ultra-Lightweight and High-Strength Cellular Structural Composites Inspired by Biomimetics," *Composites Part B: Engineering*, Vol. 121, July 2017, pp. 108–121. https://doi.org/10.1016/j.compositesb.2017.03.033
- [2] Sairajan, K. K., Aglietti, G. S., and Mani, K. M., "A Review of Multifunctional Structure Technology for Aerospace Applications," *Acta Astronautica*, Vol. 120, March 2016, pp. 30–42. https://doi.org/10.1016/j.actaastro.2015.11.024
- [3] Meola, C., Boccardi, S., and Carlomagno, G., "Composite Materials in the Aeronautical Industry," *Infrared Thermography in the Evaluation of Aerospace Composite Materials*, Vol. 1, Jan. 2017, pp. 1–24. https://doi.org/10.1016/b978-1-78242-171-9.00001-2

- [4] Su, L., Liu, H., Yao, G., and Zhang, J., "Experimental Study on the Closed-Cell Aluminum Foam Shock Absorption Layer of a High-Speed Railway Tunnel," *Soil Dynamics and Earthquake Engineering*, Vol. 119, April 2019, pp. 331–345. https://doi.org/10.1016/j.soildyn.2019.01.012
- [5] Yao, S., Xiao, X., Xu, P., Qu, Q., and Che, Q., "The Impact Performance of Honeycomb-Filled Structures Under Eccentric Loading for Subway Vehicles," *Thin-Walled Structures*, Vol. 123, Feb. 2018, pp. 360–370. https://doi.org/10.1016/j.tws.2017.10.031
- [6] Zheng, X., Fu, Z., Du, K., Wang, C., and Yi, Y., "Minimal Surface Designs for Porous Materials: From Microstructures to Mechanical Properties," *Journal of Materials Science*, Vol. 53, No. 14, 2018, pp. 10,194–10,208. https://doi.org/10.1007/s10853-018-2285-5
- [7] Christensen, J., Kadic, M., Wegener, M., Kraft, O., and Wegener, M., "Vibrant Times for Mechanical Metamaterials," MRS Communications, Vol. 5, No. 3, 2015, pp. 453–462. https://doi.org/10.1557/mrc.2015.51
- [8] Zhao, J., Li, Y., and Liu, W. K., "Predicting Band Structure of 3D Mechanical Metamaterials with Complex Geometry via XFEM. Computational Mechanics, Vol. 55, No. 4, 2015, pp. 659–672. https://doi.org/10.1007/s00466-015-1129-2
- [9] Wang, Y., Li, F., Wang, Y., Kishimoto, K., and Huang, W., "Tuning of Band Gaps for a Two-Dimensional Piezoelectric Phononic Crystal with a Rectangular Lattice," *Acta Mechanica Sinica*, Vol. 25, No. 1, 2008, pp. 65–71. https://doi.org/10.1007/s10409-008-0191-9
- [10] Ma, C., Chang, Y., Wu, S., and Zhao, R. R., "Deep Learning-Accelerated Designs of Tunable Magneto-Mechanical Metamaterials," ACS Applied Materials and Interfaces, Vol. 14, No. 29, 2022, pp. 33,892–33,902. https://doi.org/10.1021/acsami.2c09052
- [11] Chan, Y.-C., Ahmed, F., Wang, L., and Chen, W., "METASET: Exploring Shape and Property Spaces for Data-Driven Metamaterials Design," *Journal of Mechanical Design*, Vol. 143, No. 3, 2020, Paper 031707. https://doi.org/10.1115/1.4048629
- [12] Zhou, X., Xiao, Q., and Wang, H., "Metamaterials Design Method Based on Deep Learning Database," *Journal of Physics: Conference Series*, Vol. 2185, No. 1, 2022, Paper 012023. https://doi.org/10.1088/1742-6596/2185/1/012023
- [13] Dai, D., Tang, C., Zhao, D., Xia, S., and Bai, H., "Understanding a Deep Neural Network Based on Neural-Path Coding," *IEEE Access*, Vol. 8, Sept. 2020, pp. 174,495–174,506. https://doi.org/10.1109/ACCESS.2020.3024959
- [14] Maaranen, H., Miettinen, K., and Mäkelä, M. M., "Quasi-Random Initial Population for Genetic Algorithms," *Computers and Mathematics with Applications*, Vol. 47, No. 12, 2004, pp. 1885–1895. https://doi.org/10.1016/j.camwa.2003.07.011
- [15] Maaranen, H., Miettinen, K., and Penttinen, A., "On Initial Populations of a Genetic Algorithm for Continuous Optimization Problems," *Jour*nal of Global Optimization, Vol. 37, No. 3, 2006, pp. 405–436. https://doi.org/10.1007/s10898-006-9056-6
- [16] López, F., "TPOT: Pipelines Optimization with Genetic Algorithms," Towards Data Science [Online Database], Dec. 2020, https://towards datascience.com/tpot-pipelines-optimization-with-genetic-algorithms-56ec44ef6ede [retrieved 9 Sept. 2022].
- [17] Xue, T., Beatson, A., Chiaramonte, M., Roeder, G., Ash, J. T., Menguc, Y., Adriaenssens, S., Adams, R. P., and Mao, S., "A Data-Driven Computational Scheme for the Nonlinear Mechanical Properties of Cellular Mechanical Metamaterials Under Large Deformation," *Soft Matter*, Vol. 16, No. 32, 2020, pp. 7524–7534. https://doi.org/10.1039/d0sm00488j
- [18] Omairey, S. L., Dunning, P. D., and Sriramula, S., "Development of an ABAQUS Plugin Tool for Periodic RVE Homogenization," *Engineering with Computers*, Vol. 35, No. 2, 2018 pp. 567–577. https://doi.org/10.1007/s00366-018-0616-4
- [19] Xia, Z., Zhang, Y., and Ellyin, F., "A Unified Periodical Boundary Conditions for Representative Volume Elements of Composites and Applications," *International Journal of Solids and Structures*, Vol. 40, No. 8, 2003, pp. 1907–1921. https://doi.org/10.1016/s0020-7683(03)00024-6
- [20] McKay, M. D., Beckman, R. J., and Conover, W. J., "Comparison of Three Methods for Selecting Values of Input Variables in the Analysis of Output from a Computer Code," *Technometrics*, Vol. 21, No. 2, 1979, pp. 239–245. https://doi.org/10.1080/00401706.1979.10489755
- [21] Gao, J., Li, H., Luo, Z., Gao, L., and Li, P., "Topology Optimization of Micro-Structured Materials Featured with the Specific Mechanical Properties," *International Journal of Computational Methods*, Vol. 17,

- No. 3, 2019, Paper 1850144. https://doi.org/10.1142/s021987621850144x
- [22] Bostanabad, R., Chan, Y.-C., Wang, L., Zhu, P., and Chen, W., "Globally Approximate Gaussian Processes for Big Data with Application to Data-Driven Metamaterials Design," *Journal of Mechanical Design*, Vol. 141, No. 11, 2019, Paper 111402. https://doi.org/10.1115/1.4044257
- [23] Han, X., Liang, Y., Li, Z., Li, G., Wu, X., Wang, B., Zhao, G., and Wu, C., "An Efficient Genetic Algorithm for Optimization Problems with Time-Consuming Fitness Evaluation," *International Journal of Computational Methods*, Vol. 12, No. 1, 2015, Paper 1350106. https://doi.org/10.1142/s0219876213501065
- [24] Kim, Y., Kim, Y., Yang, C., Park, K., Gu, G. X., and Ryu, S., "Deep Learning Framework for Material Design Space Exploration Using

- Active Transfer Learning and Data Augmentation," *npj Computational Materials*, Vol. 7, No. 1, 2021, Paper 140. https://doi.org/10.1038/s41524-021-00609-2
- [25] Kouznetsova, V., Brekelmans, W. A. M., and Baaijens, F. P. T., "An Approach to Micro-Macro Modeling of Heterogeneous Materials," *Computational Mechanics*, Vol. 27, No. 1, 2001, pp. 37–48. https://doi.org/10.1007/s004660000212
- [26] "Sabic Innovative Plastics Ultem 1000R PEI," Songhan Plastic Technology Datasheet, Shanghai, PRC, http://www.lookpolymers.com/polymer\_SABIC-Innovative-Plastics-ULTEM-1000R-PEI.php [retrieved 18 March 2021].

R. Ohayon Associate Editor